

Magnetic topologies and two-class coronal mass ejections: a numerical magnetohydrodynamic study

W. Liu^{1,2}, X. P. Zhao¹, S. T. Wu³, and P. H. Scherrer¹

¹ W. W. Hansen Experimental Physics Laboratory, Stanford University, Stanford, CA 94305, USA

² Department of Physics, Stanford University, Stanford, CA 94305, USA

³ Center for Space Plasma and Aeronomic Research, Department of Mechanical and Aerospace Engineering, The University of Alabama in Huntsville, Huntsville, AL 35899, USA

Received 14 October 2004 / accepted 20 December 2004

Abstract. White-light observations of the solar corona show that there are two characteristic types of Coronal Mass Ejections (CMEs) in terms of speed-height profiles: so-called fast CMEs that attain high speeds low in the corona and slow CMEs that gradually accelerate from low initial speeds. Low & Zhang (2002) have recently proposed that fast and slow CMEs result from initial states with magnetic configurations characterized by normal prominences (NPs) and inverse prominences (IPs), respectively. To test their theory, we employed a two-dimensional, time-dependent, resistive magnetohydrodynamic code to simulate the expulsion of CMEs in these two different prominence environments. Our numerical simulations demonstrate that (i) a CME-like expulsion is more readily produced in an NP than in an IP environment, and, (ii) a CME originating from an NP environment tends to have a higher speed early in the event than one originating from an IP environment. Magnetic reconnection plays distinct roles in the two different field topologies of these two environments to produce their characteristic CME speed-height profiles. Our numerical simulations support the proposal of Low & Zhang (2002) although the reconnection development for the NP associated CME is different from the one sketched in their theory. Observational implications of our simulations are discussed.

Key words. *Magnetohydrodynamics* (MHD) – Sun: corona – Sun: coronal mass ejections (CMEs) – Sun: magnetic fields

1. Introduction

The accumulated observations of Coronal Mass Ejections (CMEs) obtained over more than 3 solar cycles by the coronagraphs onboard the *Skylab*, *Solar Maximum Mission*, and *Solar and Heliospheric Observatory (SOHO)* have shown two characteristic types of CME speed-height profiles: (I) so-called fast CMEs attaining high speeds above the CME median speed (400 km s^{-1}) low in the corona with little or even negative subsequent accelerations, and, (II) slow CMEs gradually accelerating from low initial speeds ($\leq 400 \text{ km s}^{-1}$) (Gosling et al. 1976; MacQueen & Fisher 1983; Dryer 1996; Sheeley et al. 1999; St. Cyr et al. 1999, 2000; Moon et al. 2002). It has also been recognized that Type I CMEs tend to originate from active regions and are frequently accompanied by flares, while Type II events usually originate away from active regions and are accompanied by eruptive prominences. Outstanding examples of these two characteristic types can be found in a given sample of CMEs, but it should be pointed out that there is a continuous spectrum of speed-height profiles between these two types as the opposite extremes. Another way to distinguish these two types of events was given by Andrews & Howard (2001). They showed that CMEs observed by the LASCO coronagraphs onboard *SOHO* may fall into two categories: Type C characterized with a constant speed and Type A characterized with a significant acceleration, which respectively correspond to Types I and II.

The underlying physics responsible for the dual character of CME speed-height profiles remains among the outstanding questions in CME research. Recently, Low & Zhang (2002, hereafter referred to as LZ02) suggested a theory to explain this phenomenon in terms of the different hydromagnetic environments in which CMEs occur. CMEs are correlated at about the 75% level with prominence eruptions (Munro et al. 1979; Webb & Hundhausen 1987; St. Cyr et al. 1999). There are two magnetic types of quiescent prominences referred to as the Normal and Inverse Prominences (Tandberg-Hanssen 1995), hereafter called NPs and IPs respectively. Low & Zhang pointed out that these two types of prominences represent different magnetic field topologies which have distinct consequences for the interplay between magnetic reconnection and CME expulsion dynamics. They gave qualitative sketches of this hydromagnetic interplay which suggest that fast and slow CMEs are naturally associated with NPs and IPs, respectively.

In the case of an NP, the surrounding field has a topology such that the CME is expelled with a current sheet to be dissipated by magnetic reconnection ahead of the erupting prominence. This reconnection is a break-out effect similar to the one originally proposed by Antiochos et al. (1999) for a multipolar magnetic field. In the LZ02 proposal, the global field is bipolar with a magnetic flux rope (Chen 1989; Chen et al. 1997). The rise of the flux rope and prominence drives break-out reconnection ahead. Reconnection produces a slingshot effect which, in turn, drives the CME and prominence. This runaway situation naturally produces a fast CME with an impulsive acceleration and flare heating early in the event. It is worth mentioning that such

a timing correlation between a fast CME and flare does not necessarily mean that the flare is driving the CME.

In contrast, an IP is associated with a magnetic-flux rope topology which produces a current sheet trailing behind the CME and erupting prominence. This current sheet is not driven directly by the CME but forms passively from the left-behind magnetic field. Magnetic reconnection is then not compelled to occur early and there is no impulsive CME acceleration or flare heating by reconnection early in the event. A CME produced in this hydromagnetic environment may be expected to be gradually accelerated from a low initial speed.

Studies of flare morphology and timing associated with fast and slow CMEs (Zhang et al. 2002; Zhang & Golub 2003) have shown that observations of this kind are consistent with the proposed theory of LZ02. Ultimately, observations of more incisive kind will be needed to verify or reject the LZ02 theory. On the other hand, the proposed theory of LZ02 is based on intuitive sketches of the relevant hydromagnetic processes. It is therefore important to perform numerical magnetohydrodynamic (MHD) simulations to directly investigate if the two distinct CME acceleration processes of LZ02 can be produced.

Individual simulation works have been reported in the literature on the acceleration of CMEs. Wu et al. (1995) and Wu et al. (1997), respectively using a 2-D and 2.5-D ideal MHD model, studied CME expulsions involving a magnetic flux rope that can be interpreted to be those representing an IP. In their models, there was no magnetic reconnection taking place. A similar study, but involving reconnection in a configuration resembling an NP, was performed by Guo et al. (1996) using a 2-D resistive code. However, the topological differences between the two types of configuration had not been recognized in connection with the two-class CMEs by these authors, nor by others until the recent work by LZ02. On the other hand, different numerical models adopted in these works (Wu et al. 1995, 1997; Guo et al. 1996) make it difficult to directly compare the CME acceleration between the two configurations from their results. Therefore a systematic, comparative simulation study of CME expulsions involving magnetic reconnection in both IP and NP configurations will be instructive in checking on the ideas of LZ02 and in an exploration of the interplay between magnetic reconnection and CME expulsion dynamics. Such a study is reported in this paper, and, as we shall see, new effects not considered by LZ02, with regard to CMEs in an NP environment, are among the results we will report. § 2 describes the numerical model. Simulation results are presented in § 3, followed by discussions on operating forces, magnetic topologies, and magnetic reconnection in § 4. Finally, we conclude this paper in § 5 with remarks relevant to the LZ02 theory and observational implications.

2. Description of the Simulation Model

The numerical model used for this study, based on those of Wu et al. (1995) and Guo et al. (1996), is composed of a set of two-dimensional, time-dependent, resistive, single-fluid MHD equations in the spherical coordinates (r, θ, ϕ) , under an axisymmetry assumption ($\partial/\partial\phi = 0$).

The governing equations, including the conservation laws of mass, momentum, and energy and the magnetic induction equation, are identical to those in Guo et al. (1996) which the interested reader is referred to for the mathematical formulation. We summarize the model as follows.

(i) The computational domain is defined as $1R_s \leq r \leq 7.14R_s$ and $-1.5^\circ \leq \theta \leq 91.5^\circ$, where R_s is the solar radius and $\theta = 0^\circ$ ($\theta = 90^\circ$) the north pole (equator). We used an $81(r) \times 63(\theta)$ grid, uniform in the meridional direction ($\Delta\theta = 1.5^\circ$) and non-uniform in the r-direction ($\Delta r_i \equiv r_i - r_{i-1} = 0.95[\Delta\theta]r_{i-1}$) for a better resolution near the solar surface, with Δr_i ranging from $0.025R_s$ at the coronal base to $0.178R_s$ at the outer boundary. The grid was staggered to prohibit sawtooth oscillations.

(ii) The MHD equations were solved by the combined difference technique (Guo et al. 1991; Wu et al. 1995). The essence of this technique is to employ different numerical schemes to treat different equations according to their physical nature. Namely, the second-type upwind scheme is used for the continuity and energy equation, the Lax scheme for the momentum equation, and the Lax-Wendroff scheme for the magnetic induction equation.

(iii) The boundary conditions are: (a) a symmetric boundary at the equator and pole, (b) linear extrapolation at the outer boundary, and (c) the method of projected normal characteristics (Wu & Wang 1987) at the inner boundary. To guarantee the solenoidal condition, viz., $\nabla \cdot \mathbf{B} = 0$, the reiterative divergence-cleaning method (Ramshaw 1983) was applied.

(iv) One of the major modifications to the previous model was that we prescribed a uniform magnetic resistivity ($\eta = 8.75 \times 10^3 \Omega \text{ m}$) throughout the whole computational domain, rather than the anomalous resistivity used by Guo et al. (1996) which favors reconnection only in regions with large electric current density. By doing this, various regions were treated equally, in view of the large difference in the current density distribution between the IP and NP configurations as we shall see in § 4. This modification is essential for a direct comparison between the two configurations.

We took three steps to simulate the expulsion of a CME in the corona, following Wu et al. (1995) and Guo et al. (1996). First we constructed an initial state of the corona with a quasi-equilibrium helmet streamer by using the relaxation method (Steinolfson et al. 1982). The resulting magnetic field, plasma flow velocity, and electric current density are shown in Figure 1 (see Fig. 1b in Wu et al. 1995 for the corresponding plasma density distribution). The characteristic parameters are listed in Table 1.

In the next step, we emerged a flux rope with various energy contents and two types of magnetic configuration from below the photosphere into the corona. Our 2-D model approximates the central cross-section of the 3-D flux rope which could be anchored at two ends on the photosphere in a realistic geometry. The gas pressure and magnetic field of the flux rope (see Equations (4) and (5) in Guo et al. 1996), in an equilibrium state, were analytically specified in local cylindrical coordinates (r', θ', z') , with Equation (5) being modified:

$$\mathbf{B}(r') = \pm \mu_0 j_0 \left(\frac{1}{2} a r' - \frac{1}{3} r'^2 \right) \mathbf{e}_{\theta'}, \quad (1)$$

where a is the radius of the flux rope. The “ \pm ” in this equation represents different senses of circulation (or polarity) of the flux rope’s magnetic field: the poloidal field in the *upper* part of the rope with a “+” (“-”) sign is of the same (opposite) circulation with respect to the external coronal field. Considering that the prominence material is presumably contained in the *lower* part of the flux rope, the “+” (“-”) therefore corresponds to an IP (NP) topology (Tandberg-Hanssen 1995). Equivalently, the azimuthal current in the emerging flux rope flows in the same direction for the “+” case as that in the vertical current sheet of the helmet streamer (Fig. 1b). To implement the emergence process, we initially placed the flux rope below the photosphere with its center at $r = R_s - a$. We then slowly displaced the rope upward at a constant speed $v_{em} (\ll v_A$, see Table 2) by accordingly changing the physical variables at the inner boundary. It took 4 hours for the flux rope to entirely emerge into the corona and then the inner boundary conditions were set back to their original form. The reader is referred to Wu et al. (1995) for a detailed mathematical treatment of this flux rope emergence process. The last step was carried out by simply letting the system evolve by itself until $t = 40$ hrs. We present the simulation results in the next section.

3. Simulation Results

A total of 8 simulation cases, grouped into 4 pairs, were performed with various sizes of the emerging flux rope. The two cases of each pair have identical physical conditions except opposite magnetic polarities of the emerging flux rope, respectively corresponding to the NP and IP topology. The energy contents (i.e., the combined magnetic and thermal energy) inside the flux rope (assuming the third-dimensional thickness $\Delta z' = 0.1R_s$ in the local cylindrical coordinates) are 1.76×10^{31} , 3.95×10^{31} , 7.02×10^{31} , and 1.10×10^{32} ergs, respectively for the 4 pairs of cases (cf. $\sim 10^{32}$ ergs needed to expel a moderately large CME, see Hundhausen 1999; Forbes 2000). We tabulate the key parameters of these cases in Table 2 and describe detailed results as follows.

Figure 2 shows the height-time and speed-time profiles of the “erupting flux rope”¹ center (defined as the O-type neutral point) for the studied cases. The solid (dotted) lines represent the cases of the NP (IP) environment. As we can see, the differences between the two types of environments are evident. In Cases 1a and 2a, the emerging flux rope has already destabilized the helmet streamer and launched a CME by the end of the simulation in the NP configuration. In contrast, the streamer and the flux rope are still in equilibrium in the IP configuration in Cases 1b and 2b. As expected from LZ02’s theory, these profiles reveal distinct characteristics between the two types of topologies: (i) an NP environment seems to be more in favor of producing CMEs than an IP environment (also see Zhang & Low 2003); (ii) a CME produced in an NP configuration tends to have a higher speed in its early life than a CME (if any) originating from an IP environment under otherwise identical conditions. We take note of that the average CME

¹ For the NP configuration, the “erupting flux rope” refers to the new flux rope formed by reconnection; for the IP configuration, it refers to the originally emerging flux rope. This will be further explained in the following text.

eruption speed in Case 4a is about 2.3 times that in Case 4b (see Table 2), which agrees well with the typical fast-to-slow speed ratios of two-class CMEs derived from the *Skylab* and recent *SOHO/LASCO* coronagraphs (e.g. 775 km s⁻¹ versus 330 km s⁻¹ in Gosling et al. 1976, and 955 km s⁻¹ versus 411 km s⁻¹ in St. Cyr et al. 1999). The other cases in this study show much higher ratios.

Let us now focus our attention on two eruptive cases — 4a (NP configuration) and 4b (IP configuration). Figure 3 shows the magnetic field and the plasma velocity for these two cases. The corresponding azimuthal electric current density, J_ϕ , and plasma density enhancement, $[\rho(r, \theta, t) - \rho(r, \theta, 0)]/\rho(r, \theta, 0)$, are respectively displayed in Figures 4 and 5.

3.1. Eruptive Case — Normal Prominence Configuration

In Case 4a, we notice that upon the flux rope emergence, a curved current sheet is developed (Fig. 4a) between the leading edge of the emerging rope and the helmet dome (i.e., the closed field region of the helmet streamer) whose bipolar magnetic field is tied on the photosphere and in a direction opposite to the field in the upper part of the flux rope. Due to the finite resistivity, magnetic reconnection occurs in the current sheet and rapidly forms a *new* flux rope between the *old* (emerging) flux rope and the helmet dome (Fig. 3a). Once this new rope is formed, the current sheet splits into two halves (Fig. 4b) and two X-type neutral points appear on the flanks of the old rope (Fig. 3b). The magnetic flux in the new rope then grows as reconnection proceeds until all the closed-field flux in the helmet dome is converted to the new rope's flux. In the meantime, the new flux rope expands and runs upward very fast while the old one follows and loses an equal amount of magnetic flux as the helmet-dome field above (Fig. 3b and 3c). Note that the old flux rope must contain sufficient poloidal flux to annihilate the closed field of the helmet dome ahead in order to set free the flux rope itself (also see LZ02). We identify the new flux rope as the main body of a CME in this numerical experiment. v_f and \bar{v} in Table 2 respectively refer to the final and average speed of the new flux rope's center for the cases of the NP configuration. At $t = 25$ hrs, the erupting material has escaped from the computational domain with an average speed of $\bar{v} = 161.0$ km s⁻¹ and the system reaches a quasi-equilibrium state (Figs. 3d and 4d) similar to the initial state (Fig. 1). We further note that, during the eruption phase (i.e., $t < 25$ hrs), the maximal current is on the flanks of the old flux rope where the current sheets are located (e.g., Figs. 4b and 4c) and the largest density enhancement occurs at the two lateral dips of the new flux rope, close to its center (the left column of Fig. 5).

3.2. Eruptive Case — Inverse Prominence Configuration

In the case of the IP configuration (Case 4b), the emerging flux rope undergoes a two-stage evolution as we can see from Figure 2: (i) a slow evolution (from 0 hrs to 7 hrs) sets in upon the flux rope emergence; (ii) the flux rope then goes unstable at around 7 hrs (exhibiting a gradual acceleration) and later propagates upward into the interplanetary space with $\bar{v} = 70.4$ km s⁻¹.

The evolution of the magnetic field and plasma velocity, electric current density, and density enhancement for Case 4b is shown in the right columns of Figures 3, 4, and 5, respectively. It is clearly noted that there is no reconnection on the leading edge of the flux rope because the magnetic field in the upper part of the rope runs in the same sense as the external field of the helmet dome. However, a vertical current sheet is formed, trailing the flux rope from below as the rope rises (e.g., Figs. 4g and 4h). Magnetic reconnection ensues and dissipates the current sheet. As a result of reconnection as well as the rising X-type neutral point due to the fixed boundary condition at the inner boundary (Wu et al. 1995), the opened magnetic field is later reclosed low in the corona, as shown in Figures 3g and 3h. This enables the helmet streamer structure to recover at ~ 40 hrs (not shown). Similar processes take place in Case 4a as well after a vertical current sheet is formed below the old flux rope (Figs. 3c and 3d). The recovery to equilibrium is much slower in the IP than in the NP configuration. This is partly due to the different CME propagation speeds and dynamic time scales for these two magnetic topologies. It is interesting to note that, in the early phase, the maxima of the electric current (Figs. 4e and 4f) and density enhancement (Figs. 5e and 5f) occur in the vertical current sheet and the lower part of the emerging flux rope, respectively, in contrast with those of Case 4a.

4. Discussions

4.1. Operating Forces

In a MHD representation of the corona plasma, there are three forces, viz., the Lorentz force, pressure gradient force, and gravitational force, which fundamentally determine the dynamics of the flux rope system (e.g., Wu et al. 1995; Guo et al. 1996; Hu & Liu 2000). We show in Figure 6 the spatial distributions in the equatorial plane of the normalized radial components of these forces for Cases 4a (left) and 4b (right) during the early stage of the simulation. By examining the forces, we notice the following interesting features.

For the NP configuration (Case 4a), the pressure force is the dominant positive force to destabilize the helmet streamer in the early stage ($t < 4$ hrs) (Figs. 6a and 6b), but it drops significantly afterwards. This is true because the emerging flux rope carries substantial mass as well as upward momentum into the helmet dome and a large pressure force is accordingly developed; after the emergence ($t > 4$ hrs) there is no more momentum being added into the corona except for the inner boundary conditions on the photosphere to maintain the background solar wind. In contrast, the Lorentz force in the newly formed flux rope is relatively small. This happens for the following reasons. On the one hand, the emerging flux rope carries a current in a direction *opposite* to that in the external helmet-streamer field and magnetic reconnection rapidly dissipates the current near the leading edge of the old flux rope around the equatorial plane. As a result, the current density in that region is very small and the current distribution peaks on the flanks of the old flux rope (Figs. 4a, 4b, and 7a through 7c). On the other hand, because reconnection gradually removes the constraints of the helmet-dome's closed field ahead of the new flux rope,

the new flux rope's material and frozen-in magnetic field can rise and expand readily (Figs. 3a and 3b), leading to a decreased magnetic field strength (Figs. 8a through 8c) and further lowering the current density as well as the pressure gradient force inside the volume of the new flux rope. Being the cross product of the current density and magnetic field strength, a small Lorentz force (Figs. 6a through 6c) is therefore produced in the new flux rope and its vicinity, in the presence of the decreased current and magnetic field.

For the IP configuration (Case 4b), the pressure gradient force and gravitational force exhibit similar behaviors and magnitudes as in Case 4a (Fig. 6). However, the Lorentz force tells us a different story. First, unlike Case 4a, the emerging flux rope in this case bears a current in the *same* direction as that of the helmet streamer above and this current produces an additional positive Lorentz force which can be understood in terms of the attractive force between the two like-signed currents. Second, there is no reconnection on the leading edge of the flux rope (cf. Case 4a) and the constraints from the overlying helmet-dome arcades cannot be readily removed. Therefore, the rise and expansion of the flux rope are suppressed by the arcades. This leads to a pileup of plasma (e.g., Fig. 5e) in the flux rope during the course of the emergence and results in an enhanced magnetic field (Figs. 8d through 8f) and current (Figs. 4e, and 7d through 7f). For these two reasons the Lorentz force appears much larger in this case compared with that in Case 4a (Figs. 6d through 6f). We also note that the Lorentz force flips its direction across the flux rope center due to the circulating magnetic field: this force is negative (downward) in the upper half of the rope, tending to hold the rising material; it switches upward in the lower half, supporting the dense plasma (Figs. 6e and 6f). This feature is less evident in Case 4a, as the Lorentz force is smaller and the topology is more complex (involving two flux ropes rather than one) in that case. As to the temporal evolution, the flux rope experiences two stages as we note in § 3.2. Early during the emergence before the center of the flux rope comes across the photosphere, the pressure gradient force is the most dominant to lift off the rope plasma; however, the Lorentz force remains negative above the center and tends to suppress the upward motion (Fig. 6e). Later on, after the center appears in the corona, the positive Lorentz force below it joins the pressure force to work against the gravity as well as the confining Lorentz force in the upper half of the rope. As the pressure force dies away after the emergence completion, the positive Lorentz force takes over the dominance. The complex interplay of these forces accounts for the slow evolution stage (< 7 hrs) of the flux rope which appears as a hump in the speed-time profile (Fig. 2b). After that, the positive Lorentz force in the lower part of the flux rope remains dominant, responsible for the gradual acceleration of the flux rope starting at $t \sim 7$ hrs, and leads to its eventual eruption.

4.2. Magnetic Topologies and Reconnection

Now comes the question why the flux rope erupts faster in the NP than in the IP configuration. We illustrate by simulation that in the NP configuration case magnetic reconnection plays a direct role in launching the CME (LZ02) by forming the new flux rope; this process removes

the closed field lines of the helmet dome as well as their constraints of the downward Lorentz force ahead of the new flux rope, thereby allowing the new flux rope to escape readily. Whereas, in the case of the IP configuration the overlying magnetic arcades tend to confine the flux rope; lacking mechanisms (e.g., reconnection) to remove the confinement, the flux rope thus fails to reach a higher initial speed. To appreciate this point, let us further examine our simulation results, focusing on the topological differences.

Firstly, the reader is reminded of the physical environment specified by this numerical study. (i) The characteristic plasma β at the bottom of the corona is unity, which means that the magnetic energy and thermal energy are comparable, and the Lorentz force and pressure gradient force are roughly of equal importance. (ii) A CME is initiated by introducing a flux rope to emerge through the photosphere into the corona. (iii) Except the magnetic polarity of the emerging flux rope, all the conditions are the same for the two cases arranged in a pair (NP and IP configuration), which implies that topology-independent forces (e.g., the pressure gradient and gravitational force) would behave similarly in the two cases but topology-dependent forces (e.g., the Lorentz force) would not.

With these points in mind we realize that, since the flux rope emergence injects a substantial amount of mass, magnetic flux, electric current and upward momentum into the corona, such a flux rope possesses a potential to disrupt the helmet streamer, where the increasing pressure gradient force would play an important role especially in the early stage of the emergence (< 2 hrs), such as in Cases 4a and 4b (Fig. 6). In the meantime, the inputted mass also induces an extra downward gravitational force that competes with the the upward pressure gradient force. The consequent evolution heavily depends on how the corona responds to such an injection during the first a few hours. Since the pressure force and gravitational force are similar in a pair of cases, we shall pay more attention on their different Lorentz force.

In Case 4a (NP configuration), for example, the flux rope emergence drives magnetic reconnection on the leading edge of the flux rope. In turn, reconnection clears the constraints ahead, i.e., the closed field lines of the helmet dome, and thus allows the flux rope to rise more readily. This is a break-out situation similar to that of Antiochos et al. (1999). Once reconnection removes all the closed field lines, the flux rope is left with an open-field channel ahead in the helmet streamer. Note that the confining Lorentz force almost vanishes in the equatorial plane above the center of the new flux rope (see Figs. 6a through 6c). Therefore, the only remaining major constraints that would prevent the flux rope from erupting now come from the gravity. Driven by the large pressure gradient force, the flux rope can thus overcome the gravitational pull and readily escape along the open-field channel with a high initial speed.

Nevertheless, in the IP configuration case (e.g., Case 4b), there is no reconnection on the leading edge of the flux rope to remove the overlying arcades and the corona responds to the flux rope emergence with a negative Lorentz force above the flux rope center, much larger than its counterpart in the corresponding NP configuration case (e.g., Figs. 6d through 6f). This confining Lorentz force, together with the gravity, overcomes part of the upward momentum and tends to

suppress the emergence against the pressure gradient force. Incidentally, it is worth mentioning that although the magnitude of the negative Lorentz force is not large in comparison with the more dominant gravity, when the pressure force and gravity are in competition at some critical point, even a small additional force would easily turn the lever of force competition to one end. In this sense, the negative Lorentz force plays such a crucial role. This results in the hump-shaped portion in the speed-time profiles for the IP configuration cases (see Fig. 2b). Losing a significant amount of momentum in the very early stage of the emergence, the flux rope fails to be driven to a high initial speed even with the positive Lorentz force coming into play later on.

The other NP and IP configuration cases show similar behaviors of the forces as in Cases 4a and 4b, respectively. As the radius and emergence speed of the flux rope become smaller, less upward momentum is injected into the corona, and thus it is more difficult to work against the gravitational pull. Depending on the energetics of the emergence, the flux rope may erupt at a lower speed (e.g., Cases 1a and 3b) or even fail to escape (e.g., Cases 1b and 2b).

In brief, in the NP configuration cases, the fast CMEs result from the flux rope eruptions mainly driven by the pressure gradient force, with little magnetic confinement; in the IP configuration cases, the slow CMEs are driven by the pressure gradient force and positive Lorentz force in the lower half of the flux rope, subject to the significant drags from the confining Lorentz force above the flux rope center. This explains the distinct speed-time profiles of CMEs in the two topologically different types of cases.

5. Concluding Remarks

We have presented MHD simulations in the form of the flux rope emergence to investigate the relationship between magnetic topologies and two-class CMEs as suggested by LZ02. In conclusion, our numerical results demonstrate that: (i) A CME-like expulsion is more readily produced in an NP than in an IP environment, under otherwise the same conditions. This agrees with the results from the analytical calculations of magnetic energy storage in the two types of prominences given by Zhang & Low (2003). (ii) Early in the event, a CME originating from an NP environment tends to have a higher initial speed low in the corona while a CME from an IP environment tends to experience a slow evolution and then erupt with a lower initial speed and gradual acceleration. (iii) One of the ratios of the average CME speeds for these two types of magnetic topologies is about 2.3, consistent with the observations reported by Gosling et al. (1976) and St. Cyr et al. (1999). (iv) In an NP environment, magnetic reconnection occurs on the leading edge of the emerging flux rope. This reconnection removes the magnetic confining force produced by the closed external field ahead of the flux rope and launches a fast CME in a manner similar to the Magnetic Break-out Model (Antiochos et al. 1999). However, in an IP environment, with reconnection absent on the leading edge and subject to the magnetic confinement from the overlying arcades, the emerging flux rope either fails to erupt (e.g., Cases 1b and 2b) or results in a slow CME (e.g., Case 4b), similar to the early works given by Wu et al. (1995) and Wu et al.

(1997). Reconnection, taking place in the vertical current sheet trailing the rising flux rope, is a passive effect of the CME expulsion². In this sense, magnetic reconnection plays a principal role in generating a fast CME in the NP configuration but does not in the IP environment (Zhang et al. 2002).

On the whole, the present study qualitatively agrees well with the LZ02 scenario. However, for an NP configuration, the slingshot topology predicted by LZ02 is not present in our simulations and the new flux rope formed by reconnection, as clearly shown in our results, was not considered in their theory. The reason to account for this difference may be explained as follows. To produce a slingshot topology (see Fig. 2 in LZ02), one must expect that reconnection occurs at a single X-type neutral point on top of the flux rope and as a result the pre-event, closed external field lines of the helmet dome reconnect with the internal field lines of the flux rope to form a “slingshot”. In our time-dependent simulations, as soon as the emerging flux rope touches the overlying helmet-dome field, a current sheet forms in between and the tearing mode instability may set in due to the prescribed finite resistivity. This may produce many small magnetic islands which may rapidly coalesce to form larger islands and eventually the new flux rope. This new flux rope sits between the emerging rope and the helmet dome, and on the flanks are the two X-type neutral points where subsequent reconnection occurs. We propose that, depending on the reconnection development which is difficult to predict in advance, both the slingshot topology (as in LZ02) and the topology with a new flux rope formed (as in our simulations) might be the case in a realistic solar environment, and both topologies would be in favor of producing fast CMEs.

It should be pointed out that, although the CMEs are generated by emerging flux ropes into the corona somewhat artificially in this numerical experiment, this paper is not aimed to investigate the initiation mechanisms of CMEs which have been addressed elsewhere in the literature (e.g., Forbes 2000; Wu et al. 2000; and references therein). However, regardless of CME initiations, the topology-dependent behavior of the CME expulsion indeed reveals the logical connection between the magnetic topologies and the two types of CME speed-height profiles, which is the main goal of this study.

The CME speeds in our simulations are systematically lower than observed values. One of the reasons is that we traced the center of the erupting flux rope to obtain the corresponding CME speed, which is an underestimate because an observed CME speed is usually measured at the bright CME front that gains an additional speed due to the self-expansion of the flux rope relative to its center. Another reason is that the initial energy content in the emerging flux rope is not large enough to launch a fast CME up to 800 km s^{-1} . This deficiency could be remedied by seeking low- β MHD solutions or by upgrading this 2-D model to a 2.5-D or a full 3-D one, consequently increasing the energy content. These attempts would be beyond the scope of the present paper. It is worth noting that Wu et al. (2004), alternatively, have adopted a 2.5-D model

² Note that reconnection here does remove a small portion of the flux from the overlying, closed field in the helmet dome by converting it to the flux in the outer layers of the flux rope.

and simulated both fast and slow CMEs (at speeds comparable to observed values) in an IP configuration, by invoking one or a combination of the three driving mechanisms: magnetic flux injection, mass drainage, and additional heating. This suggests that the two-class CME speed-height profiles could result from a variety of mechanisms among which the scenario of LZ02 was an initiative example. We would expect that even faster CMEs will be produced if an NP configuration is considered by Wu et al. (2004).

Observations, as always, will be needed to assess a theory or a numerical study. Several aspects in the LZ02 theory and in our simulations are observationally testable. One prediction of the LZ02 theory is that magnetic reconnection, taking place either above or below the flux rope, plays distinct roles in the different field topologies of the two prominence environments. Solar flares, which are observational manifestations of reconnection, are hence expected to exhibit distinct timing and morphological behaviors in association with fast and slow CMEs. Such behaviors have recently been reported by Zhang et al. (2002) and Zhang & Golub (2003) using *TRACE* UV/EUV observations. Hard X-ray (HXR) emissions produced by accelerated particles during flares provide another tool to shed light on the magnetic topology of the reconnection site and the current sheet (Sui & Holman 2003). One can test whether there exist different morphologies of flares associated with the two types of CMEs, using HXR data obtained by *RHESSI* (Lin et al. 2002) or the Hard X-ray Telescope onboard the *Yohkoh* satellite. In particular, for limb flares, HXR images of the loop-top (LT) source, which is presumably located near/at the reconnection site, can be compared with H_{α} images to check whether the LT occurs above or below the erupting prominence (if any), and to see whether such an occurrence is associated with a fast or slow CME, respectively.

In the case of an NP environment, a new flux rope is formed by reconnection ahead of the old flux rope. If the remainder of the magnetic flux in the old flux rope is significant, the CME would contain two flux ropes with opposite chiralities of the magnetic field. This aspect of our simulations may be tested by using *in situ* observations of the magnetic configurations in the interplanetary counterparts of Earth-directed CMEs, provided that the chiralities of the flux ropes are conserved during their interplanetary propagation. The January 10–11, 1997 magnetic cloud (MC) observed by the *WIND* spacecraft contained ${}^4\text{He}^{++}/\text{H}^{+}$ abundance similar to that of the streamer belt material, suggesting an association between the MC and a helmet streamer. In addition, a very cold region of exceptionally high density was detected at the rear of the MC, and this dense region had an unusual composition, indicating an association with the prominence material. This event was interpreted to be associated with a CME on January 06, 1997 with an estimated speed of 450 km s^{-1} observed by *SOHO/LASCO* (Burlaga et al. 1998). The very cold region also contained a magnetic configuration, very likely of a flux rope, though its size was much less than the MC. We suggest that, by respectively fitting the observed magnetic field of the MC and the very cold region with a flux rope model, their chiralities can be determined and thus will provide observational evidence to test our simulation results. Recently, multiple MCs have been reported by Wang et al. (2003). The March 03–05, 2001 MCs, one of the three events

in their study, consisted of two flux ropes with opposite chiralities, one right-handed and the other left-handed. They interpreted these two MCs as a consequence of two successive CMEs with projected speeds of 313 km s^{-1} and 631 km s^{-1} , respectively. However, identifying the solar origin of a MC has its uncertainty and it was possible that the two MCs might result from a single fast CME. If this is the case, such events would provide observational supports to our model. It will be interesting to see, statistically, whether two successive MCs are associated with a single CME or successive CMEs and we look forward to such kind of observational tests to check on our simulations.

Ultimately, observations of the magnetic field will provide more incisive information to verify or reject the LZ02 theory. A study using line-of-sight MDI magnetograms is in progress in order to determine if there are differences in the magnetic environments of the source regions of the two types of CMEs (M. Zhang & J. Burkepile, private communication). In the meantime, advance in measuring the magnetic field in the corona by polarimetric methods (Lin et al. 1998; Judge 1998; Lin et al. 2000; Trujillo Bueno 2001; Trujillo Bueno et al. 2002) will be able to put the theory to a direct test in the near future.

Acknowledgements. Work performed by WL, XPZ and PHS was supported at Stanford University by NASA grants NAGW 2502 and NAG5-10483, NSF grant ATM 9400298, and ONR grant N0014-97-1-0129. Work performed by STW was supported by NASA grant NAG5-12843 and NSF grant ATM-0316115.

References

- Andrews, M. D., & Howard, R. A. 2001, *Space Sci. Rev.*, 95, 147
- Antiochos, S. K., DeVore, C. R., & Klimchuk, J. A. 1999, *ApJ*, 510, 485
- Burlaga, L. F., et al. 1998, *J. Geophys. Res.*, 103, 277
- Chen, J. 1989, *ApJ*, 338, 453
- Chen, J. et al. 1997, *ApJ*, 490, L191
- Dryer, M. 1996, *Sol. Phys.*, 169, 421
- Forbes, T. G. 2000, *J. Geophys. Res.*, 105, 23153
- Gosling, J. T., Hildner, E., MacQueen, R. M., Munro, R. H., Poland, A. I., & Ross, C. L. 1976, *Sol. Phys.*, 48, 389
- Guo, W. P., Wang, J. F., Yao, Y. Q., & Liang, B. X. 1991, *Chinese J. Space Sci.*, 11, 168
- Guo, W. P., Wu, S. T., & Tandberg-Hanssen, E. 1996, *ApJ*, 469, 944
- Hundhausen, A. J. 1999, in *The Many Faces of the Sun*, ed. K. Strong, J. Saba, B. Haisch, & J. Schmelz (New York: Springer), 143
- Hu, Y. Q., & Liu, W. 2000, *ApJ*, 540, 1119
- Judge, P. G. 1998, *ApJ*, 500, 1009
- Lin, H., Penn, M. J., & Kuhn, J. R. 1998, *ApJ*, 493, L978
- Lin, H., Penn, M. J., Tomczyk, S. 2000, *ApJ*, 541, L83
- Lin, R. P., et al. 2002, *Sol. Phys.*, 210, 3

Low, B. C., & Zhang, M. 2002, *ApJ*, 564, L53

MacQueen, R. M., & Fisher, R. R. 1983, *Sol. Phys.*, 89, 89

Moon, Y.-J., Choe, G. S., Wang, H., Park, Y. D., Gopalswamy, N., Yang, G., & Yashiro, S. 2002, *ApJ*, 581, 694

Munro, R. H., et al. 1979, *Sol. Phys.*, 61, 201

Ramshaw, J. D. 1983, *J. Comp. Phys.*, 52, 592

Sheeley, N. R., Jr., Walters, J. H., Wang, Y.-M., & Howard, R. A. 1999, *J. Geophys. Res.*, 104, 24739

St. Cyr, O. C., Burkepile, J. T., Hundhausen, A. J., & Lecinski, A. R. 1999, *J. Geophys. Res.*, 104, 12493

St. Cyr, O. C., et al. 2000, *J. Geophys. Res.*, 105, 18169

Steinolfson, R. S., Suess, S. T., & Wu, S. T. 1982, *ApJ*, 255, 730

Sui, L., & Holman, G. D. 2003, *ApJ*, 596, L251

Tandberg-Hanssen, E. 1995, *The Nature of Solar Prominences* (Dordrecht: Kluwer)

Trujillo Bueno, J. 2001, in *ASP Conf. Ser. 236, Advanced Solar Polarimetry: Theory, Observations, and Instrumentation*, ed. M. Sigwarth (San Francisco: ASP), 161

Trujillo Bueno, J., Landi Degl'Innocenti, E., Collados, M., Merenda, L., & Manso Sainz, R. 2002, *Nature*, 415, 403

Wang, Y. M., Ye, P. Z., Wang, S. 2003, *J. Geophys. Res.*, 108, 1370

Webb, D. F., & Hundhausen, A. J. 1987, *Sol. Phys.*, 108, 383

Wu, S. T., Guo, W. P., & Dryer, M. 1997, *Sol. Phys.*, 170, 265

Wu, S. T., Guo, W. P., Plunkett, S. P., Schmieder, B., & Simnett, G. M. 2000, *J. Atmo. and Solar-Terr. Phys.*, 62, 1489

Wu, S. T., Guo, W. P., & Wang, J. F. 1995, *Sol. Phys.*, 157, 325

Wu, S. T., & Wang, J. F. 1987, *Comp. Method Appl. Mech. Eng.*, 64, 267

Wu, S. T., Zhang, T. X., Tandberg-Hanssen, E., Liu, Y., Feng, X., Tan, A. 2004, *Sol. Phys.*, accepted

Zhang, M., & Golub, L. 2003, *ApJ*, 595, 1251

Zhang, M., Golub, L., DeLuca, E., & Burkepile, J. 2002, *ApJ*, 574, L97

Zhang, M., & Low, B. C. 2004, *ApJ*, 600, 1043

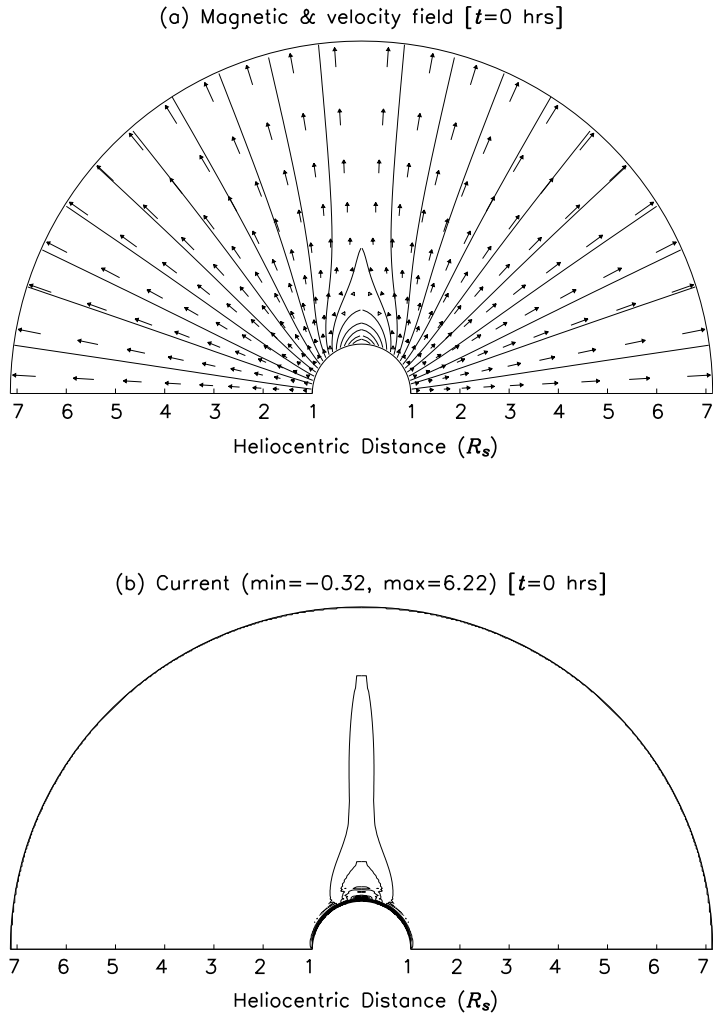


Fig. 1. The initial state of the solar corona with a helmet streamer over the equator: (a) the magnetic field lines and solar wind velocity; (b) spatial distribution of the azimuthal current density J_ϕ (in contours). The minimum and maximum are shown on top of Panel b in units of $J_0 = 2.29 \times 10^{-7} \text{ A m}^{-2}$ and 18 contour levels are uniformly set between these extrema. Note the vertical current sheet extending upward from the helmet streamer cusp.

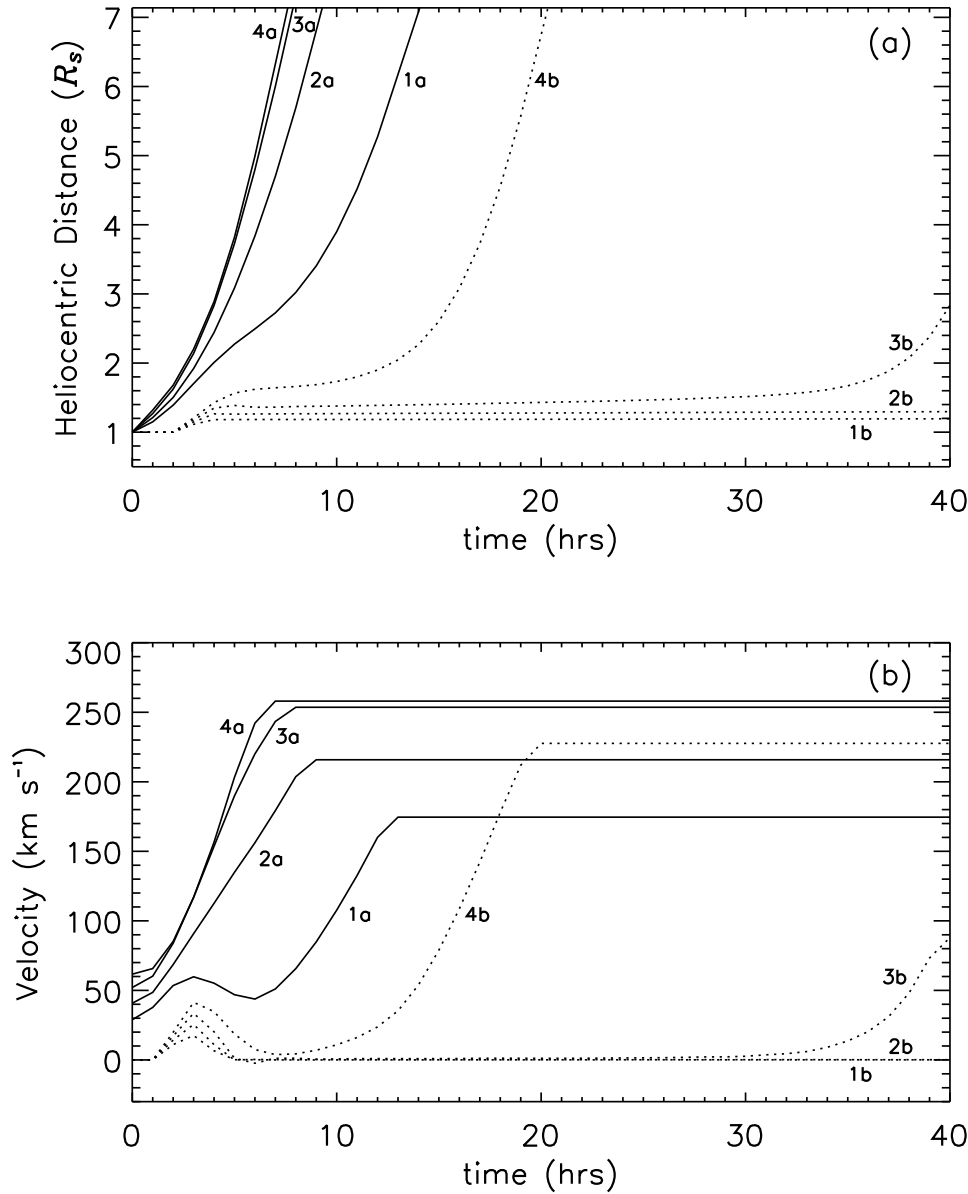


Fig. 2. (a) Height-time and (b) speed-time profiles of the center of the “erupting flux rope”¹ for the eight cases listed in Table 2. The solid (dotted) lines correspond to the cases with the NP (IP) configuration. Note that for the speed profiles in Panel b: the initial humps at $t \sim 3$ hrs are results of the flux rope emergence; the final flat portions (except for Cases 1b and 2b) are extrapolations of the speeds evaluated at the boundary ($r = 7.14R_s$); also the final portions of curves 1b and 2b overlap each other.

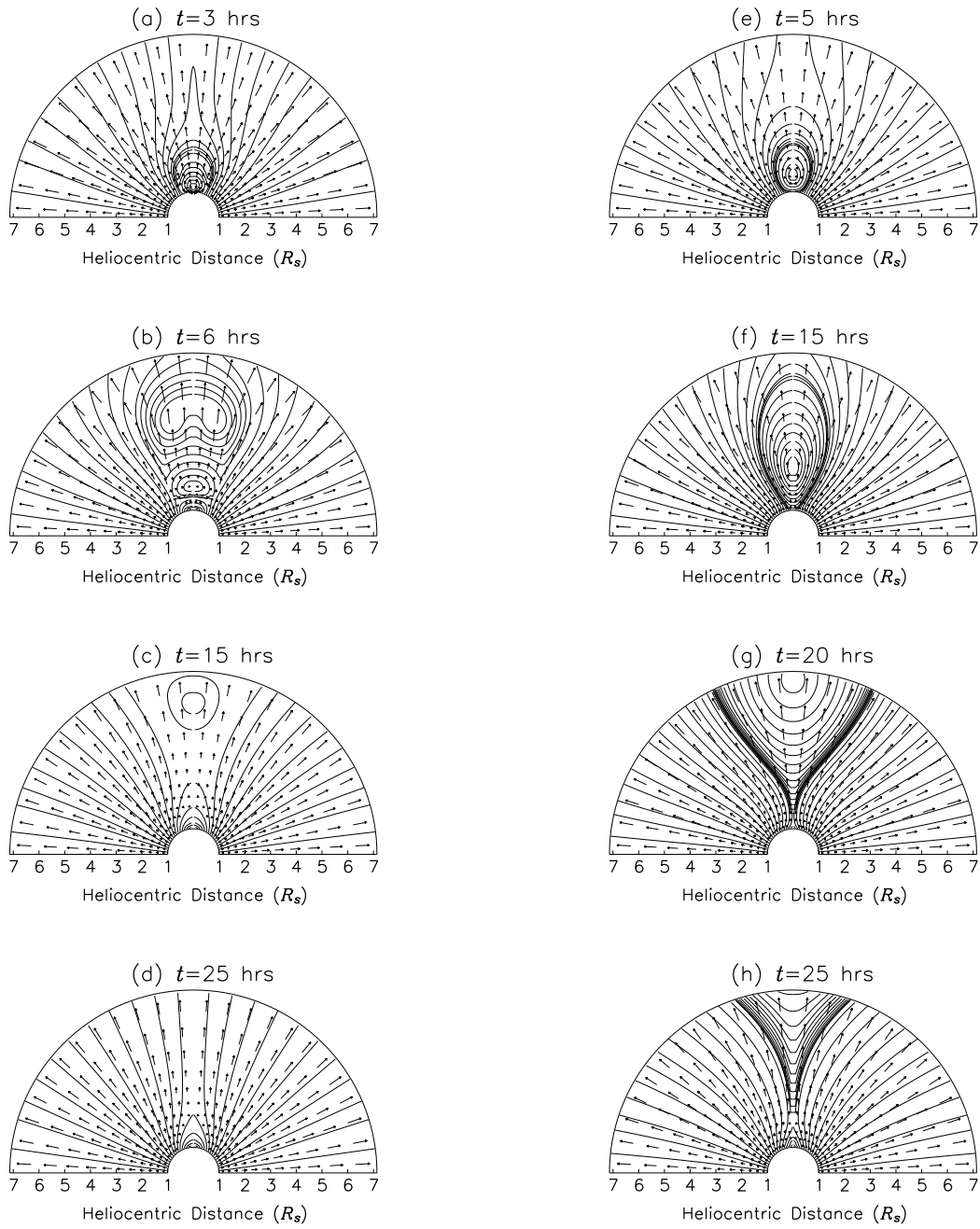


Fig. 3. Temporal evolution of the magnetic field and plasma flow velocity for Case 4a (NP configuration, left column) and Case 4b (IP configuration, right column).

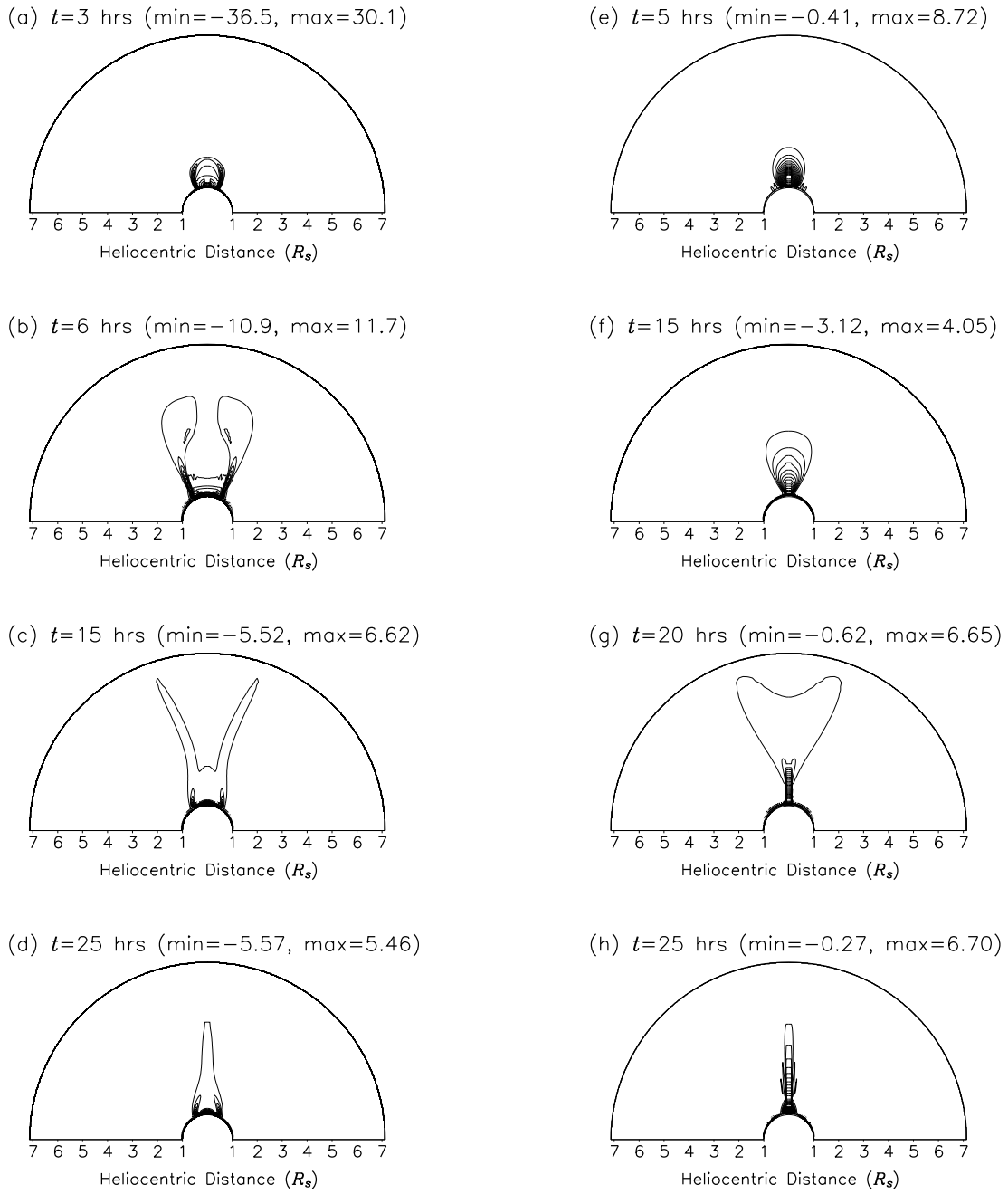


Fig. 4. The corresponding contours of the azimuthal electric current density J_ϕ (in units of $J_0 = 2.29 \times 10^{-7} \text{ A m}^{-2}$) of Figure 3. The minima and maxima are shown on top of each panel and the intervals [min, max] are evenly divided into 38 and 34 contour levels for Cases 4a (left) and 4b (right), respectively.

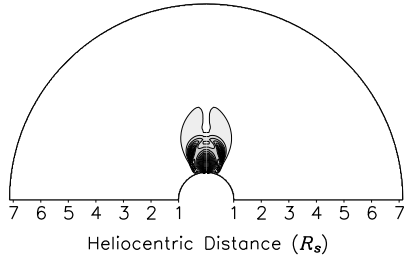
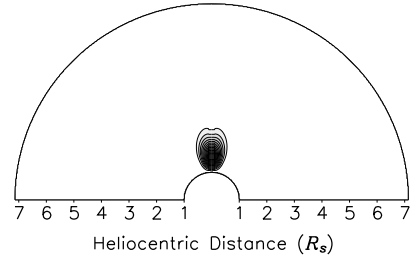
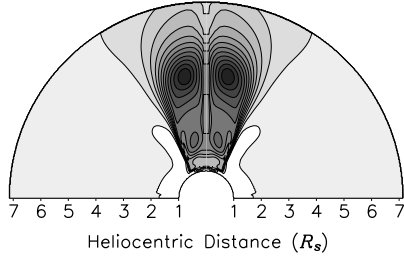
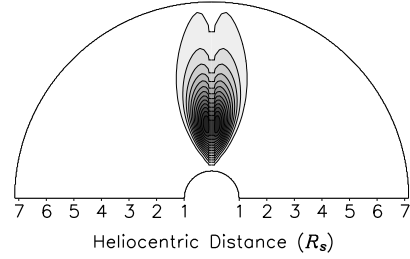
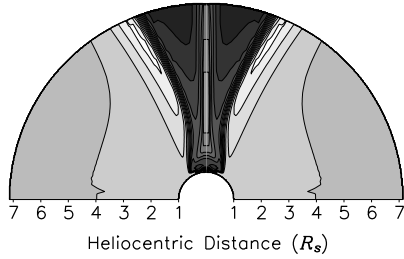
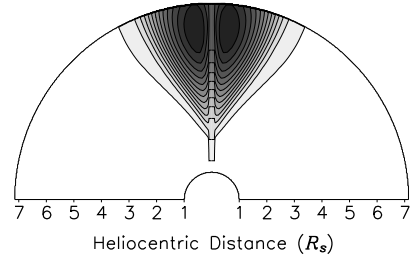
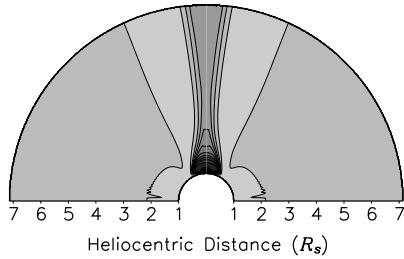
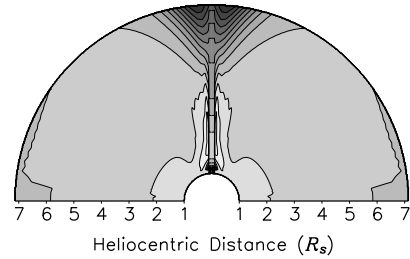
(a) $t=3$ hrs (min=-0.04, max=7.88)(e) $t=5$ hrs (min=-0.09, max=10.7)(b) $t=6$ hrs (min=-0.32, max=4.49)(f) $t=15$ hrs (min=-0.34, max=8.68)(c) $t=15$ hrs (min=-0.30, max=0.97)(g) $t=20$ hrs (min=-0.28, max=6.99)(d) $t=25$ hrs (min=-0.28, max=0.73)(h) $t=25$ hrs (min=-0.36, max=1.49)

Fig. 5. The corresponding relative density enhancement, i.e., $[\rho(r, \theta, t) - \rho(r, \theta, 0)]/\rho(r, \theta, 0)$, of Figure 3, plotted in the same manner as Figure 4 except that here are 15 contour levels filled with gray scale shades (bright: low, dark: high).

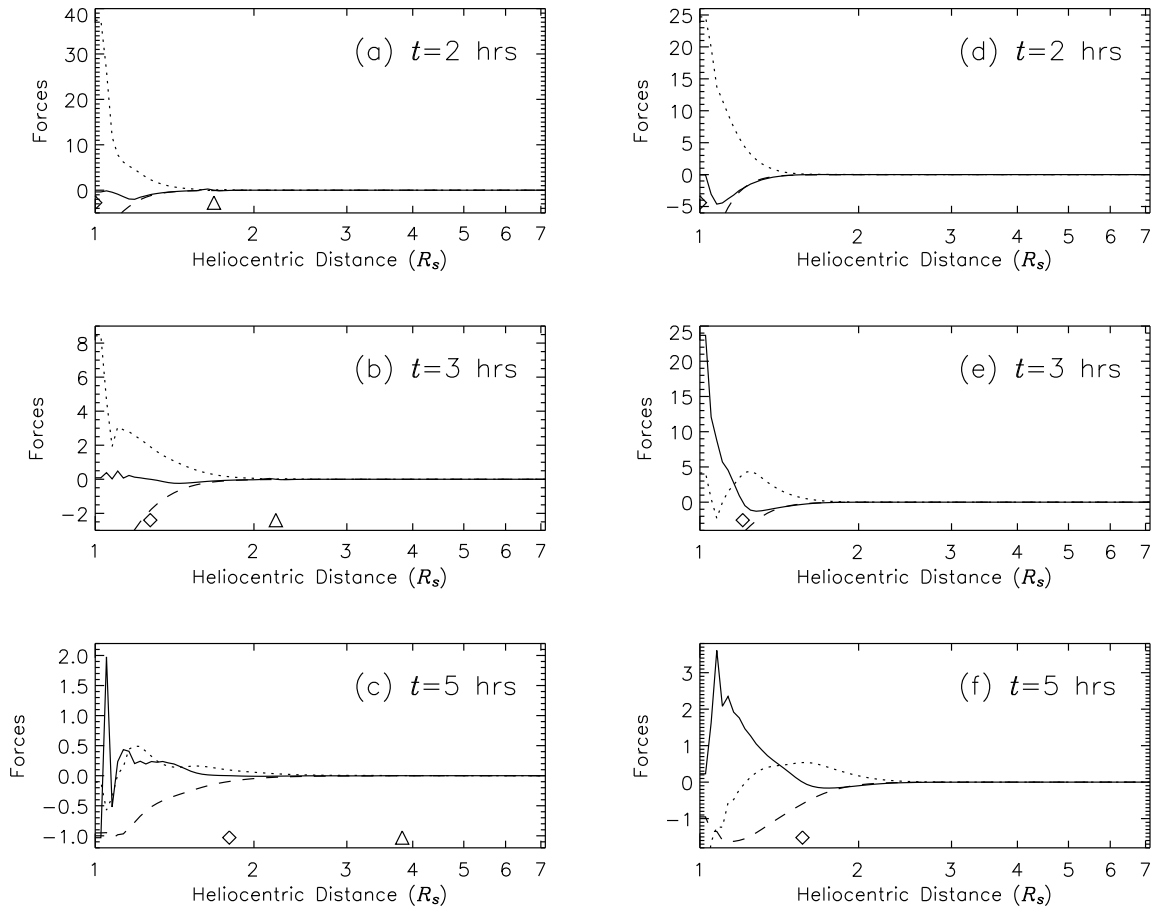


Fig. 6. Radial components of the forces (i.e., Lorentz force —, pressure gradient force, and gravitational force - - -) per unit volume as functions of the heliocentric distance in the equatorial plane at various times for the NP (Case 4a, left column) and IP (Case 4b, right column) configuration. Distance is logarithmically plotted to show details near the solar surface. All the forces are normalized by the gravitational force at the equator on the photosphere in the initial state. Note the flux rope center (i.e., the O-type neutral point) in each case. Diamond symbols denote the radial positions of the center of the originally emerging flux rope; triangles mark those of the new flux rope formed by reconnection in the case of the NP configuration.

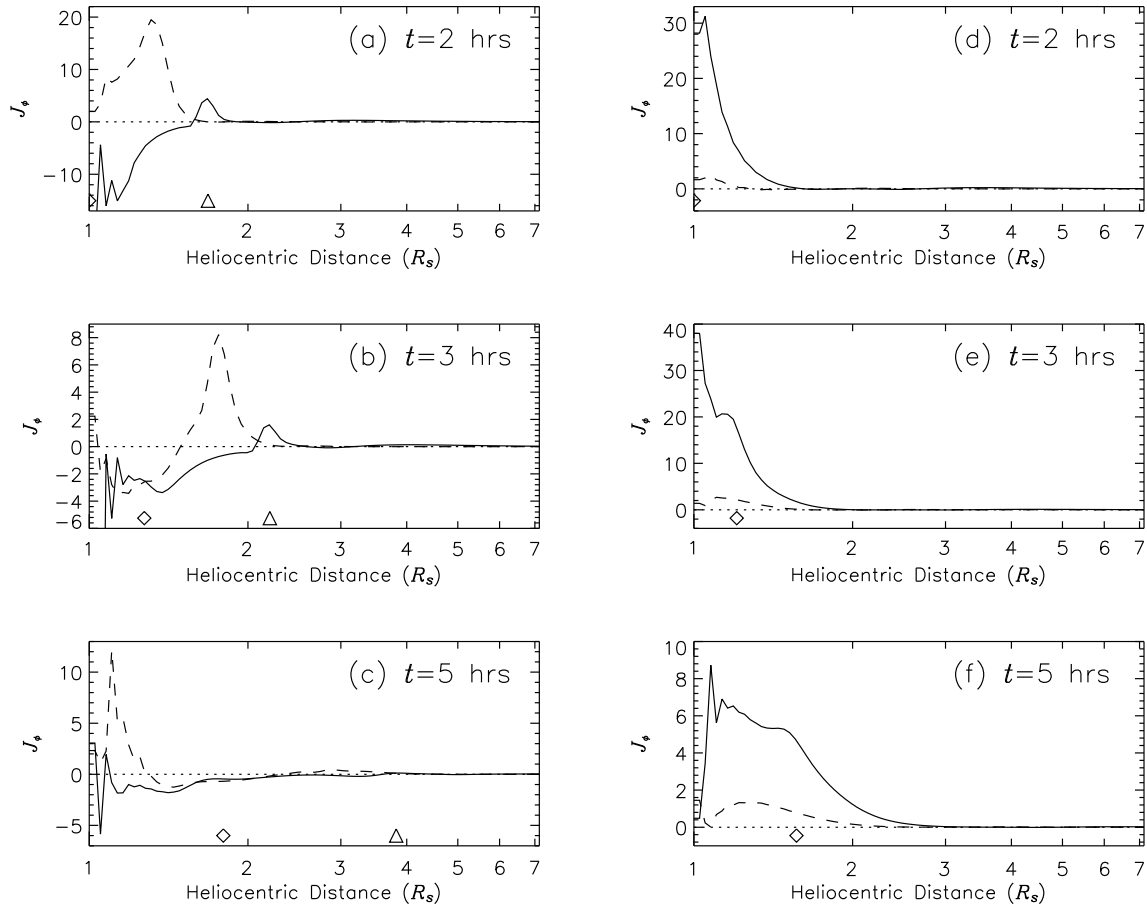


Fig. 7. Azimuthal current density distribution, J_ϕ (in units of $J_0 = 2.29 \times 10^{-7} \text{ A m}^{-2}$) at various times corresponding to Figure 6, in the equatorial plane ($\theta = 90^\circ$, solid lines) and along $\theta = 72^\circ$ (or $\theta = 108^\circ$, dashed lines) where the split current sheets in Case 4a are roughly located. The dotted line in each panel marks the zero level.

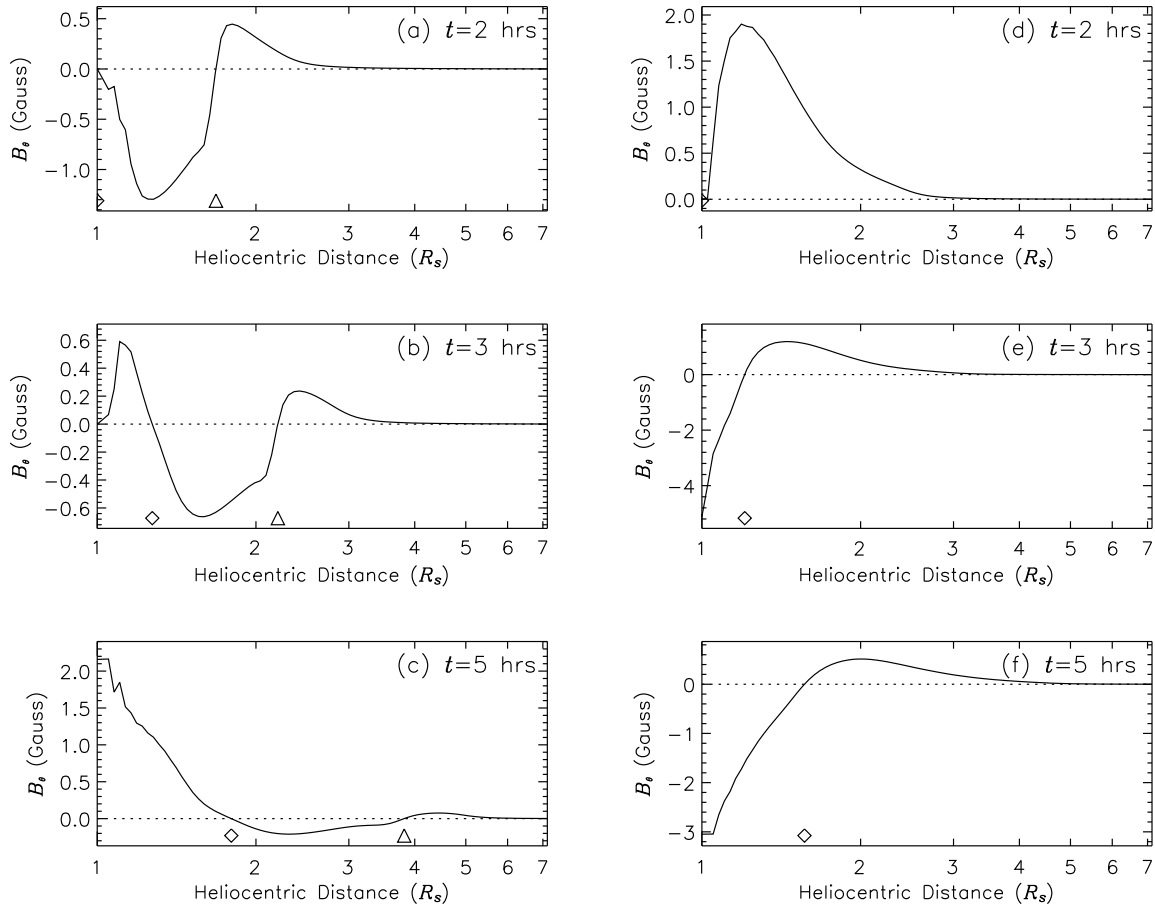


Fig. 8. θ -component of the magnetic field (B_θ) vs. heliocentric distance in the equatorial plane ($\theta = 90^\circ$) at various times, corresponding to Figure 6. The dotted lines mark the zero levels. Note that B_r vanishes at $\theta = 90^\circ$ under the symmetric boundary condition.

Table 1. Characteristic parameters of the initial state.

n_0 (electron number density)	$3.2 \times 10^8 \text{ cm}^{-3}$
T_0 (temperature)	$1.8 \times 10^6 \text{ K}$
B_0 (magnetic induction strength)	2.0 G
β_0 (plasma β)	1.0
c_s (sound speed)	176.7 km s^{-1}
v_A (Alfvén speed)	243.9 km s^{-1}
v_{sw} (solar wind speed)	209.7 km s^{-1}

Note. — All the quantities refer to the condition in the equatorial plane. The solar wind speed is evaluated at the outer boundary and the others at the inner boundary.

Table 2. Characteristics of studied cases.

Cases	$a^{(a)}$ (R_s)	Field ^(b)	Energy ^(c) (10^{31} ergs)	$v_{em}^{(d)}$ (km s^{-1})	$v_f^{(e)}$ (km s^{-1})	$\bar{v}^{(f)}$ (km s^{-1})
1a	0.10	NP	1.76	9.7	174.6	90.0
2a	0.15	NP	3.95	14.5	215.8	133.9
3a	0.20	NP	7.02	19.3	253.6	152.6
4a	0.25	NP	11.0	24.2	258.0	161.0
1b	0.10	IP	1.76	9.7	0.1	1.0
2b	0.15	IP	3.95	14.5	0.2	1.5
3b	0.20	IP	7.02	19.3	88.0	9.3
4b	0.25	IP	11.0	24.2	227.6	70.4

^(a) The radius of the emerging flux rope.

^(b) Magnetic field topologies in terms of NP or IP configurations.

^(c) The combination of the thermal and magnetic energy in the volume of the emerging flux rope, assuming the third-dimensional thickness $\Delta z' = 0.1R_s$.

^(d) The flux rope emergence speed in Step 2 as described in § 2.

^(e) The final speed of the center of the “erupting flux rope”¹. This speed is evaluated at the end of the simulation (40 hrs) or at the time when the flux rope center reaches the outer boundary of the computational domain, whichever occurs first.

^(f) The average speed of the “erupting flux rope”¹ center over the time interval during which the center remains in the computational domain.